Journal of Materials Chemistry A

ROYAL SOCIETY OF CHEMISTRY

PAPER

View Article Online
View Journal

Cite this: DOI: 10.1039/d6ta00700g

Extending the electrochemical stability window of $Ti_3C_2T_z$ MXenes *via* Ta–Hf co-substitution for durable proton exchange membrane fuel cell catalyst supports

Haridas Parse,†[a] Danielle Sviri Belilty,†[a] Bar Favelukis,[a] Mathias Krämer,[b] Andrea M. Mingers,[b] Sukanta Chakrabartty,[a] Noam Eliaz,[a] Baptiste Gault,‡[b] Dierk Raabe,[b] Maxim Sokol[a] and Brian A. Rosen*[a]

MXenes are an emerging class of two-dimensional transition metal carbides with attractive electrical conductivity, surface chemistry tunability, and high surface area, making them promising candidates for electrocatalyst support materials in proton exchange membrane fuel cells. However, their practical use at positive electrochemical potentials is severely limited by rapid and irreversible oxidative degradation. Here, we demonstrate that introducing chemical disorder through oxyphilic metal co-substitution is an effective strategy to extend the electrochemical stability window of $Ti_3C_2T_z$ MXenes. Hafnium- and tantalum–hafnium co-substituted MAX phases were synthesized and converted to corresponding MXenes, enabling systematic investigation of single and co-substitution effects. X-ray photoelectron spectroscopy reveals that Ta–Hf co-substitution suppresses titanium oxide formation and stabilizes the surface chemistry of the MXene. Electrochemical corrosion measurements show that the corrosion potential of optimized Ta–Hf co-substituted MXenes shifts positively by up to 94 mV relative to pristine $Ti_3C_2T_z$, accompanied by reduced anodic currents and delayed passivation. *Operando* element-resolved dissolution measurements further confirm suppressed metal leaching under anodic polarization. When employed as catalyst supports in proton exchange membrane fuel cells (PEMFCs), Pt-loaded Ta–Hf co-substituted MXenes exhibit significantly improved durability during accelerated stress testing. Specifically, the co-substituted MXene showed only a 9 mV degradation, whereas the pristine MXene degraded by 39 mV. Additionally, Ta–Hf MXenes demonstrate superior stability under anode reversal conditions, outperforming both unsubstituted and singly substituted MXenes. These results establish oxyphilic metal co-substitution as a general materials design strategy for stabilizing MXenes under anodic conditions, enabling their application as durable catalyst supports in advanced fuel cell systems.

Received 24th January 2026
Accepted 30th March 2026

DOI: 10.1039/d6ta00700g

rsc.li/materials-a

Introduction

The increase in global energy demand has drawn widespread attention to alternative technologies, including polymer electrolyte membrane fuel cells (PEMFCs).[1,2] Due to their high efficiency and low emissions, PEMFCs have garnered significant attention for their ability to directly convert green fuels, such as hydrogen, into electricity thereby reducing the dependence on fossil fuels.[3] Traditionally, platinum (Pt) and Pt-based alloys have been the most commonly used electrocatalysts for PEMFCs because they offer high exchange current density, chemical stability, and substantial work function.[3,4] In most cases, catalysts[2] used for PEMFCs are supported by conductive and nanoporous carbons.[5–7] Carbon-supported noble-metal-based catalysts demonstrate high activity and are considered the standard for advancements in fuel cell durability. However, carbon supports suffer from corrosion at potentials above 1.1 V *vs.* RHE due to the parasitic oxidation of the carbon support to CO_2, which decreases the durability and lifetime of the fuel cell.[8–10] This degradation of the support is particularly evident during the frequent start-up and shut-down operations that mobile fuel cells endure, as opposed to stationary fuel cells.[11,12] Therefore, to improve the lifetime and durability of PEMFC fuel cells, the development of alternative support materials is highly desirable, as addressing catalyst-support degradation is essential for their practical implementation in PEMFCs.[13]

In the past decade, transition metal carbides (TMCs) have received significant attention as a class of electrocatalyst

[a]*Department of Materials Science and Engineering, Tel Aviv University, Tel Aviv, 69987001, Israel. E-mail: barosen@tauex.tau.ac.il*

[b]*Max Planck Institute for Sustainable Materials, Düsseldorf 40237, Germany*

† Equal contribution.

‡ Present address: Univ Rouen Normandie, CNRS, INSA Rouen Normandie, Groupe de Physique des Matériaux, UMR 6634, F-76000 Rouen, France.

support material due to their high chemical stability in acidic environments, corrosion resistance, and excellent electrical conductivity.[1,14] MXenes, a class of 2D transition metal carbides, have gained significant interest in the electrocatalysis community in the field of energy storage and conversion.[15,16] MXene synthesis has often been carried out using selective engraving of the A-layer of the MAX phases $M_{n+1}AX_n$.[16–18] The general stoichiometric formula of MXene is written as $M_{n+1}X_nT_z$ where T_z represents the surface functional groups such as –O, –OH or –F, *etc.*[19–22] To date, more than fifty distinct MXenes have been successfully prepared and reported.

Among MXenes, $Ti_3C_2T_z$ has gained the greatest attention owing to its relative ease of preparation, high surface area, high electrical and thermal conductivity, versatile intrinsic properties, hydrophilicity, and electrochemical activity.[23–28] $Ti_3C_2T_z$ undergoes oxidative degradation in a wide variety of environments, including atmospheric exposure,[29,30] exposure to an oxidative gas[31] or liquid[32] or a positive electrochemical potential.[33] The mechanism of oxidation depends highly on the type of oxidative exposure and the physical state of the MXene.[34] The electrochemical oxidation of multilayer MXene flakes was studied in different electrolytes.[33,35] The corrosion behavior of single- and few-layer $Ti_3C_2T_z$ flakes were investigated in acidic electrolyte (1 M H_2SO_4), demonstrating that oxidation initiates at potentials above 0.3 V *versus* the saturated calomel electrode (SHE) and accelerates rapidly with increasing potential. It has been demonstrated that extensive anodic oxidation converts $Ti_3C_2T_z$ into electrochemically inactive TiO_2, causing severe loss of capacitance, whereas controlled low-potential partial oxidation preserves active Ti–C sites while creating enlarged interlayer spacing and nanoscale porosity. As a result, partial oxidation markedly enhances ion transport and high-rate electrochemical performance.[32,33]

The challenge is therefore to design MXene which has an extended electrochemical window of stability over which its functionality is retained and oxidation is controlled.[28] Among the strategies to achieve this goal is to substitute oxyphilic species at the M-site which can alter how the MXene flakes react under oxidative electrochemical conditions. Expanding the electrochemical window can therefore increase the number of applications for which MXenes can be used as electrocatalysts or electrocatalyst supports.

To control the electrochemical oxidation of $Ti_3C_2T_z$, single and multi-transition-metal substitutions were introduced into $Ti_3C_2T_z$ MXenes derived from triple transition metal-substituted 312 MAX phases.[30–32] Moreover, single transition metal atom substitution improve the electrochemical oxidation performance but usually provide only limited resistance to electrochemical oxidation.[36] The multiple transition metal-substituted MAX phases are the most widespread solid solutions.[37,38] Altering the MAX phases and MXenes by substituting different transition metal atoms can improve or customize their optical, electronic, thermal, mechanical, and electrochemical properties.[39–42]

Herein, we have studied the electrochemical oxidation of $Ti_3C_2T_z$ before and after 5 at% and 10 at% hafnium (Hf) and tantalum–hafnium (Ta–Hf) co-substitution (for example, $Ti_{2.85}Ta_{0.075}Hf_{0.075}C_2T_z$ and $Ti_{2.7}Ta_{0.15}Hf_{0.15}C_2T_z$) in 0.5 M H_2SO_4 at oxidizing potentials above the reversible hydrogen electrode (RHE). Ta and Hf elements can form strong metal–carbon and metal–oxygen bonds within the MXene skeleton, thereby improving the material's stability and preventing oxidative degradation in corrosive environments.[43] Moreover, Ta and Hf are very well known for the formation of a stable protective oxide layer.[44] Furthermore, the influence of the Ta and Hf co-doping in the MXene significantly improved the durability of the PEMFCs catalyst support. Multi-substituted MXenes increases the chemical variety of MXenes which can be studied, and therefore, work such as this which show synergy between multiple substitutions can encourage future studies using other variations.

Experimental section

Materials

Titanium (Ti, 99.8%), aluminum (Al, 99.7%), and lithium fluoride (LiF, 99.7%), powders were acquired from Strem Chemicals and utilized as is. Tantalum (Ta), titanium carbide (TiC), and hafnium (Hf) were procured from Alfa Aesar. Hexachloroplatinic acid ($H_2PtCl_6 \cdot 6H_2O$, >37.5% Pt) was obtained from Merck. Hydrochloric acid (HCl, 32%), sulfuric acid (H_2SO_4, 95–98%), isopropanol (IPA), and ethylene glycol (EG), were sourced from Lab-Chem. SIGRACET GDL 28BC carbon paper gas diffusion layer (GDL) and a single-sided Pt/C-coated Nafion NR-212 membrane, and a 20% Nafion solution, were purchased from Ion-Power (USA). Deionized (DI) water generated by a Milli-Q system was used in all experiments and the electrochemical study.

Ti_3AlC_2, $Ti_{3-x}Hf_xAlC_2$ and $Ti_{3-2x}Ta_xHf_xAlC_2$ MAX phase synthesis

Ti_3AlC_2 synthesis

TiC, Ti, Ta, Hf and Al powders were used to synthesize MAX phases with Hf and Ta–Hf co-substitution such as Ti_3AlC_2, $Ti_{3-2x}Hf_xAlC_2$, and $Ti_{3-2x}Ta_xHf_xAlC_2$. Initially, Ti_3AlC_2 was synthesized using a molar ratio of 2 : 1 : 1.15 for TiC : Ti : Al. The powders were mixed using ball milling (5 min at 1800 rpm) to obtain a homogeneous mixture. 5 g of the resulting mixture was cold-pressed into 20 mm diameter pellets under a uniaxial pressure of 50 MPa. The resulting pellet was placed in an alumina boat with an alumina lid and transferred to the tubular furnace for high-temperature synthesis. The pellet was annealed at 1500 °C (heating rate: 5 °C min^{-1}) for 2 h in a protective atmosphere using argon (Ar) with a 200 sccm flow rate and a small amount of Ti powder, which served as a sacrificial oxidizing agent to prevent undesired oxidation of the MAX phase. The pellet was then crushed and ball-milled at 1800 rpm to obtain a powder with a uniform particle size of 25 μm. Finally, the resulting powder was stirred overnight in HCl (9 M) and washed with DI water several times to avoid the impurities, and the final product was verified as Ti_3AlC_2.

$Ti_{3-x}Hf_xAlC_2$ and $Ti_{3-2x}Ta_xHf_xAlC_2$ synthesis

Synthesis of the phases substituted with Hf and Hf–Ta were prepared using a similar procedure as outlined above. To obtain

targeted solid MAX phases of $Ti_{2.85}Hf_{0.15}AlC_2$, $Ti_{2.7}Hf_{0.3}AlC_2$, $Ti_{2.85}Ta_{0.075}Hf_{0.075}AlC_2$ and $Ti_{2.7}Ta_{0.15}Hf_{0.15}AlC_2$ (312 MAX phases), powders of TiC, Ti, Ta, Hf, and Al were mixed in the molar ratios given in Table 1.

MXene synthesis

The synthesis of MXenes $Ti_3C_2T_z$, $Ti_{2.85}Hf_{0.15}C_2T_z$, $Ti_{2.7}Hf_{0.3}C_2T_z$, $Ti_{2.85}Ta_{0.075}Hf_{0.075}C_2T_z$ and $Ti_{2.7}Ta_{0.15}Hf_{0.15}C_2T_z$, were carried out using selective etching of the Al layer from the as-synthesized Ti_3AlC_2, $Ti_{2.85}Hf_{0.15}AlC_2$, $Ti_{2.7}Hf_{0.3}AlC_2$, $Ti_{2.85}Ta_{0.075}Hf_{0.075}AlC_2$, and $Ti_{2.7}Ta_{0.15}Hf_{0.15}AlC_2$ parent MAX phases. Typically, 500 mg of the Ti_3AlC_2 MAX phase was added to a solution comprising 800 mg of LiF and 10 mL of concentrated HCl and stirred at 45 °C in an oil bath for 24 h. Similarly, Hf-substituted MXene were synthesized. For Ta–Hf co-substituted Max phases, 500 mg of Ta–Hf co-substituted MAX phase powder was mixed to the solution containing 2000 mg of LiF and 30 mL of concentrated HCl and vigorously stirred at 45 °C for 24 h. Etching conditions for pristine Ti_3AlC_2 differ from the Ta–Hf co-substituted MAX phases due to the changes in the bonding environment. Co-substitution of Ti with Ta and Hf alters the M–A bonding. This co-substitution increases the overall stability of the MAX phases and reinforce the interaction between Al layer and transition metal layer. Therefore, the co-substituted MAX requires a higher concentration *in situ* generated HF to successfully remove the Al layer to yield corresponding MXenes.[45] After the etching process, the resulting mixture was washed with deionized (DI) water and spun down in a centrifuge at 7500 rpm for 5 minutes per cycle until the pH of the supernatant reached 7. The supernatant was collected, sonicated in an ice-cold bath sonicator for 30 min, followed by another round of centrifugation at 7500 rpm for 30 min. The resulting supernatant contained single flakes of $Ti_3C_2T_z$, $Ti_{2.85}Hf_{0.15}C_2T_z$, $Ti_{2.7}Hf_{0.3}C_2T_z$, $Ti_{2.85}Ta_{0.075}Hf_{0.075}C_2T_z$ or $Ti_{2.7}Ta_{0.15}Hf_{0.15}C_2T_z$. Vacuum filtration (Celgard 3105) was used on the supernatant to prepare free-standing films.

Table 1 Precursor molar ratios for targeted MAX phase synthesis

	Molar ratio of the elements				
Sample name	Ti	Al	TiC	Ta	Hf
Ti_3AlC_2	1	1.15	2	—	—
$Ti_{2.85}Hf_{0.15}AlC_2$	0.85	1.15	2	—	0.15
$Ti_{2.7}Hf_{0.3}AlC_2$	0.7	1.15	2	—	0.3
$Ti_{2.85}Ta_{0.075}Hf_{0.075}AlC_2$	0.85	1.15	2	0.075	0.075
$Ti_{2.7}Ta_{0.15}Hf_{0.15}AlC_2$	0.7	1.15	2	0.15	0.15

Synthesis of $Pt/Ti_3C_2T_z$, $Pt/Ti_{2.85}Hf_{0.15}C_2T_z$, $Pt/Ti_{2.7}Hf_{0.3}C_2T_z$, $Pt/Ti_{2.85}Ta_{0.075}Hf_{0.075}C_2T_z$ and $Pt/Ti_{2.7}Ta_{0.15}Hf_{0.15}C_2T_z$

Platinum (Pt) was loaded onto the surface of the MXenes at a mass of 40 wt% using the polyol method. Specifically, 45 mg of MXenes such as $Ti_3C_2T_z$, $Ti_{2.85}Hf_{0.15}C_2T_z$, $Ti_{2.7}Hf_{0.3}C_2T_z$, $Ti_{2.85}Ta_{0.075}Hf_{0.075}C_2T_z$ and $Ti_{2.7}Ta_{0.15}Hf_{0.15}C_2T_z$ was taken in a 50 ml centrifuge tube, followed by 2 mL of $H_2PtCl_6 \cdot 6H_2O$ (30 mg mL^{-1}) solution was added. The mixtures were sonicated for 15 min (Scheme 1).

Afterwards, 50 mL of EG was added to the above mixture and purged with N_2 gas for 15 minutes, after which the mixture was placed in a bath sonicator for 1 h. The resulting solution was transferred to a three-necked round-bottom flask and refluxed at 160 °C for 2 *h* under a protective nitrogen atmosphere, with vigorous stirring in an oil bath. After cooling to room temperature, the obtained powders were washed several times with an ethanol–water mixture (40 : 10 v/v) using a centrifuge at 7000 rpm for 5 min for each cycle and finally washed with pure ethanol. The obtained Pt/MXene powders were dried overnight at 80 °C and used for further studies.

Structural and chemical characterization

The PANalytical diffractometer (Aeris research edition) with a Cu Kα X-ray radiation source ($\lambda = 1.5406$ Å) in the range of 5–70° 2θ with a step size of ~0.01087° 2θ and scan speed ~0.0557° 2θ per sec was used to obtain the XRD patterns. The JEOL (IT200) and Quanta 200FEGESEM scanning electron microscope (SEM) with an energy-dispersive spectroscopy (EDS) detector was used to investigate the microstructure and the elemental analysis of the prepared samples. Atomic-scale characterization of the MAX lamellae FIB samples was carried

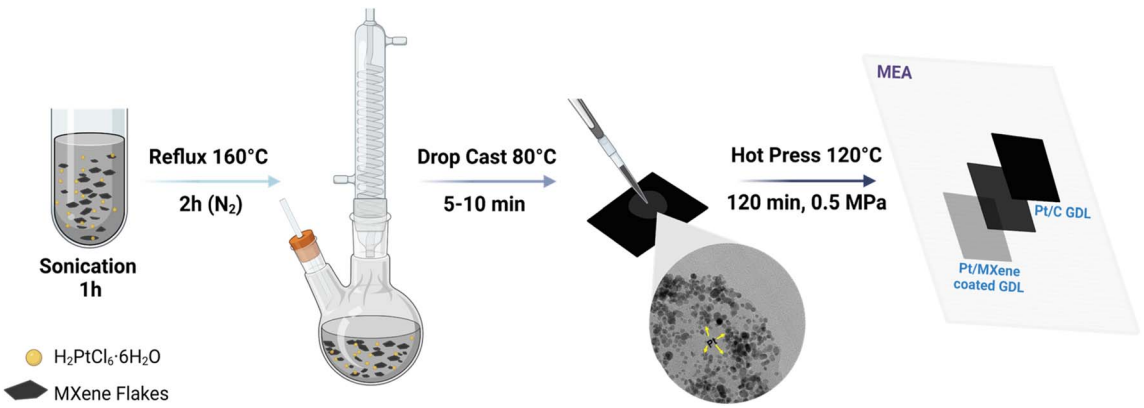

Scheme 1 Schematic representation of the synthesis of the Pt/MXene using polyol method. Created with https://www.biorender.com/.

out by high-resolution scanning transmission electron microscopy (HR-STEM), using a Cs-corrected (S-CORR) probe operating at 200 kV (Thermo Fisher Scientific Spectra 200). TEM and STEM modes using a high-angle annular dark field (HAADF) detector were used to record the material images. The EDS spectra were collected with a Super-X (Thermo Fisher Scientific) silicon drift detector (SDD). The images and the EDS spectra were processed with Thermo Fisher Scientific Velox software (version 3.14).

X-ray photoelectron spectroscopy (XPS) measurements were carried out under ultra-high vacuum (UHV) conditions with a base pressure of 2.5×10^{-10} Torr, using a 5600 Multi-Technique System (PHI, USA). The samples were irradiated with an Al Kα monochromatic source (1486.6 eV), and the emitted electrons were analyzed with a Spherical Capacitor Analyzer equipped with a 0.8 mm slit aperture. The binding energy scale was calibrated to C1s peak at 284.8 eV. Spectra were fitted using mixed Gaussian–Lorentzian line shapes after Shirley background subtraction. Peak deconvolution was performed using constraints on peak positions, area ratios, and spin–orbit splitting based on literature values.

Operando element-resolved dissolution measurements

Operando electrochemical experiments were performed using a scanning flow cell (SFC) connected to a potentiostat (ref. 600, Gamry Instruments) and an inductively coupled plasma-mass spectrometer (ICP-MS, NexION 300X, PerkinElmer) for time- and potential-resolved analysis of dissolved ion concentrations (47Ti, 178Hf, 181Ta). The SFC, consisting of 400 μm V-shaped channels with the electrolyte outlet connected to the ICP-MS, was pressed with 200 mN onto the free-standing MXene films used as the working electrode, exposing a geometric area of approximately 0.178 mm^2. A Pt tube (0.38 mm diameter) was used as the auxiliary electrode and placed in the inlet channel, while a silver–silver chloride (Ag/AgCl) electrode in 3 M KCl positioned in the outlet channel served as the reference electrode. A 0.1 M H_2SO_4 electrolyte was prepared from H_2SO_4 (96%, Merck) and deionized water (PureLab Flex2, Elga, 18 MΩ cm^{-1}, TOC < 3 ppb), and pumped with a flow rate of approximately 170 μL min^{-1} through the cell. Due to the high dissolution of Hf and Ta, these elements were electronically diluted using the band pass mass filter of the Dynamic Reaction Cell of the ICP-MS. The electrochemical protocol started with a 600 s open-circuit potential (OCP) hold, after the sample was brought into contact with the electrolyte. The potential was then ramped to 1.2 V *vs.* RHE at a scan rate of 1 mV s^{-1}.

Electrochemical measurements

The Biologic VSP-300 potentiostat was used to examine the electrochemical performance of the synthesized MXenes. Electrochemical corrosion studies were carried out using a typical three-electrode system with 0.5 M H_2SO_4 as the electrolyte. As-prepared materials coated on a glassy carbon (GC) rotating disk electrode (RDE, area = 0.19625 cm^2) were used as the working electrode. The working electrode was prepared using the drop-casting method. A freshly prepared 20 μl MXene colloidal solution (0.2 g l^{-1}) was drop-cast onto a cleaned GC disk coated with diamond slurry and subsequently dried at room temperature. An Ag/AgCl saturated KCl electrode and a Pt wire were employed as the reference and auxiliary electrodes, respectively. The potentiodynamic oxidation studies of all the MXenes were carried out by varying the potential from 0.2 to 1.2 V *vs.* RHE at a potential sweep rate of 0.167 mV s^{-1}. Open-circuit potential (OCP) tests were performed for 3 h prior to each measurement to ensure system equilibrium.

The electrochemical oxidation of MXenes carried out using three electrode system. Where, as synthesized MXene flakes drop casted on the gold coated TEM grid and wrapped in the Pt mesh and used as working electrode. The electrochemical oxidation carried out at the potential range of 0 to 0.9 V *vs.* RHE with the scan rate of 0.167 mV s^{-1} in 0.5 M H_2SO_4. The Pt wire and Ag/AgCl used as counter and reference electrode. Further, TEM images were acquired before and after electrochemical oxidation to evaluate the morphological changes and degradation pattern.

An electrochemical quartz crystal microbalance (EQCM) with a QSD-300 (Biologic) was used to investigate mass changes during electrochemical oxidation. A 4 μg MXene-loaded quartz crystal coated with Au/Ti (10 MHz frequency and sensitivity of 0.0815 ng Hz^{-1} cm^{-2}) was used as the working electrode. A platinum wire and Ag/AgCl, saturated KCl electrode served as the auxiliary and reference electrode, respectively. All the experiments were carried out in 0.5 M H_2SO_4 electrolyte solution.

Membrane electrode assembly (MEA)

The gas diffusion electrodes (GDEs) were fabricated using 5 cm^2 square-shaped carbon paper. As obtained catalysts Pt/$Ti_3C_2T_z$, Pt/$Ti_{2.85}Hf_{0.15}C_2T_z$, Pt/$Ti_{2.85}Hf_{0.30}C_2T_z$, Pt/$Ti_{2.85}Ta_{0.075}Hf_{0.075}C_2T_z$, and Pt/$Ti_{2.7}Ta_{0.15}Hf_{0.15}C_2T_z$ were used to fabricate the anodes for PEM-FC. Typically, 4 mg of each catalyst was dispersed in 1 ml of a solution comprising IPA, water, and Nafion in a 1 : 1 : 0.01 volume ratio. To obtain homogenous dispersion, the mixture was sonicated for 30 min in an ice-cold bath sonicator. The microporous layers of carbon paper were drop-casted with the resulting catalyst dispersion and dried on a hot plate at 80 °C. A commercially available Pt/C catalyst coated Nafion NR-212 membrane (0.3 mg Pt cm^{-2}) was employed as the cathode, while blank carbon paper (5 cm^2) was used on the back side of the Pt/C coated catalyst as a support. The Pt loading of all GDEs was maintained at 0.3 mg cm^{-2}. Further, hot-pressing was used to fabricate the membrane electrode assembly (MEA) by pressing the GDEs and the NR-212 membrane at 120 °C for 120 seconds under 1 MPa.

The 850e fuel cell test workstation (Scribner Associates Inc., North Carolina, USA) was used to evaluate the fuel cell performance. A full cell assembly consists of a 5 cm^2 working area of the commercial single-fuel cell, with PTFE gaskets of 230 μm thickness at the cathode and anode. Measurements of the fuel cell were recorded at a working temperature of 80 °C, with oxygen (O_2, 0.2 L min^{-1}) provided as oxidant to the cathode and humidified hydrogen (H_2, 0.2 L min^{-1}) supplied to the anode as fuel. Subsequently, the cell was conditioned using a break-in process before each measurement. The break-in process

involved cycling the cell potential consecutively between 0.6 V (2 min) and 0.35 V (2 min).

PEM fuel cell testing

Finally, accelerated stress tests (AST) and anode reversal tests were performed with a Biologic VSP-300 to evaluate the stability of catalysts such as Pt/$Ti_3C_2T_z$, Pt/$Ti_{2.85}Ta_{0.075}Hf_{0.075}C_2T_z$, and Pt/$Ti_{2.7}Ta_{0.15}Hf_{0.15}C_2T_z$. The ASTs were performed at an operating temperature of 80 °C with a supply of fully humidified H_2 and N_2 to the anode and cathode, respectively. The stability test consisted of 20 000 (20 k) cycles using chronoamperometric technique, cycling between a holding potential of 0.6 V (3 seconds) and 0.9 V (3 seconds). The stability of each catalyst was assessed by comparing polarization curves recorded before and after the 20 k cycles.

Results and discussion

Structural characterization of MAX phases

XRD analysis was carried out to determine the crystallographic properties and phase of the $Ti_{3-x}Hf_xAlC_2$- and $Ti_{3-2x}Ta_xHf_xAlC_2$-type MAX phases with different Hf and Ta compositions (for Hf doping $x = 0.15$, 0.3 and for Ta–Hf co-doping $x = 0.075$ and 0.15). Fig. 1 shows the comparative X-ray powder diffractograms of Ti_3AlC_2, $Ti_{2.85}Ta_{0.075}Hf_{0.075}AlC_2$, $Ti_{2.7}Ta_{0.15}Hf_{0.15}AlC_2$, $Ti_{2.85}Hf_{0.15}AlC_2$ and $Ti_{2.7}Hf_{0.3}AlC_2$. As-synthesized pristine Ti_3AlC_2 shows good agreement with previously reported XRD pattern in literature.[46,47] Fig. 1(b) reveals a clear shift in peaks (as represented by the dominant (104) reflection) towards lower 2θ angles due to lattice expansion upon substitution of Ti with larger atom Hf and Ta (5d element) with larger electronic cloud.[36] XRD also confirms that the substituted MAX phases retained the same structure as the pristine material, with only a small amount of secondary TiC phase (PDF-01-089-3828) indicated by an asterisk in Fig. 1(a). Fig. S1 shows the XRD patterns of synthesized free-standing $Ti_3C_2T_z$, $Ti_{2.85}Hf_{0.15}C_2T_z$, $Ti_{2.7}Hf_{0.3}C_2T_z$ $Ti_{2.85}Ta_{0.075}Hf_{0.075}C_2T_z$, and $Ti_{2.7}Ta_{0.15}Hf_{0.15}C_2T_z$ MXene films, which confirm the basal plane alignment and 2D carbide crystal structure.[48,49] Moreover, it confirms the absence of the other crystalline phases (Fig. S1). Unlike MAX phases, the shift of the (002) peak for $Ti_{2.7}Ta_{0.15}Hf_{0.15}C_2T_z$ and $Ti_{2.85}Ta_{0.075}Hf_{0.075}C_2T_z$ samples is mainly attributed to variations in the interlayer water content, consistent with the hydration-sensitive (002) reflection of $Ti_3C_2T_z$ MXene rather than a fundamental change in the MXene crystal lattice.[50]

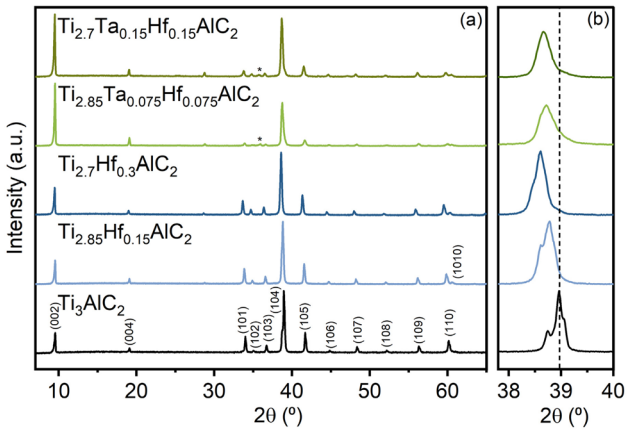

Fig. 1 XRD analysis. (a) Comparative XRD patterns of as-prepared powders targeted to MAX phase ($Ti_{3-x}Hf_xAlC_2$), ($Ti_{3-2x}Ta_xHf_x$)3AlC2 with change in Ta and Hf content ($x = 0$, 0.075, 0.15, and 0.3). (* indicate TiC; secondary phase) (b) zoomed in portion of high intensity peak at 2θ value of 30–41°, which depict the expansion of the lattice parameter.

Morphology and atomic structure characterization of MAX phases

The SEM, high-resolution scanning electron microscopy (HR-SEM), TEM, and STEM were all used to investigate the morphology and atomic structure of $Ti_{2.85}Ta_{0.075}Hf_{0.075}AlC_2$, $Ti_{2.7}Ta_{0.15}Hf_{0.15}AlC_2$, $Ti_{2.85}Hf_{0.15}AlC_2$ and $Ti_{2.7}Hf_{0.3}AlC_2$. Fig. S2 shows SEM images of the Hf-substituted MAX phases, where a representative layered structure was observed resembling pristine Ti_3AlC_2. The lateral distribution of Ta and Hf in the as-prepared Ta–Hf co-substituted MAX phases was confirmed using SEM-EDS as well as TEM-EDS analysis, as revealed in Fig. S3–S5.

The co-substituted $Ti_{2.7}Ta_{0.15}Hf_{0.15}AlC_2$ MAX phase was studied using various microscopic techniques to learn about the atomic structure and cross-sectional distribution of the substituting atoms. A typical layered MAX phase morphology of $Ti_{2.7}Ta_{0.15}Hf_{0.15}AlC_2$ was confirmed by HR-SEM in Fig. 2(a).[51] Moreover, clear visuals of the atomic layers of $Ti_{2.7}Ta_{0.15}Hf_{0.15}AlC_2$, observed from the [010] zone axis, were provided by STEM and are shown in Fig. 2(b). The *Z*-contrast between the inner and outer layers of the substituted carbides was observed using HAADF imaging, as depicted in Fig. 2(b). Further, the inset of Fig. 2(b) shows the selected-area electron diffraction (SAED) pattern, corroborating the crystallographic planes identified by XRD in Fig. 1(a).

Interestingly, the line profile in Fig. 2(c and d) shows that Ti and Hf were present in approximately equal amounts among the metal layers of the MAX phase (*i.e.*, had no preferential partitioning), whereas Ta was strongly concentrated within the middle metal layer. Previous studies by the co-authors have reported selective Ta distribution in the middle layer; however, here it is shown that this effect is unchanged even with the addition of Hf to the MXene (which did not show the segregation effect).[52] Such a differentiation may lead to differential chemical properties of the co-substituted MXenes as the relative amounts of Hf and Ta are changed.[34]

Structural and chemical characterization of MXenes

TEM and STEM were used to analyze the atomic structure of the $Ti_{2.7}Ta_{0.15}Hf_{0.15}C_2T_z$, the MXene with the largest level of substitution among the materials studied. Fig. 3(a) reveals the single few flakes of the $Ti_{2.7}Ta_{0.15}Hf_{0.15}C_2T_z$, which follow the morphology characteristic of reported MXenes.[53] STEM analysis of single-flake $Ti_{2.7}Ta_{0.15}Hf_{0.15}C_2T_z$ shown in Fig. 3(b) occurrence emphasizes the lateral distribution of the Ta and Hf

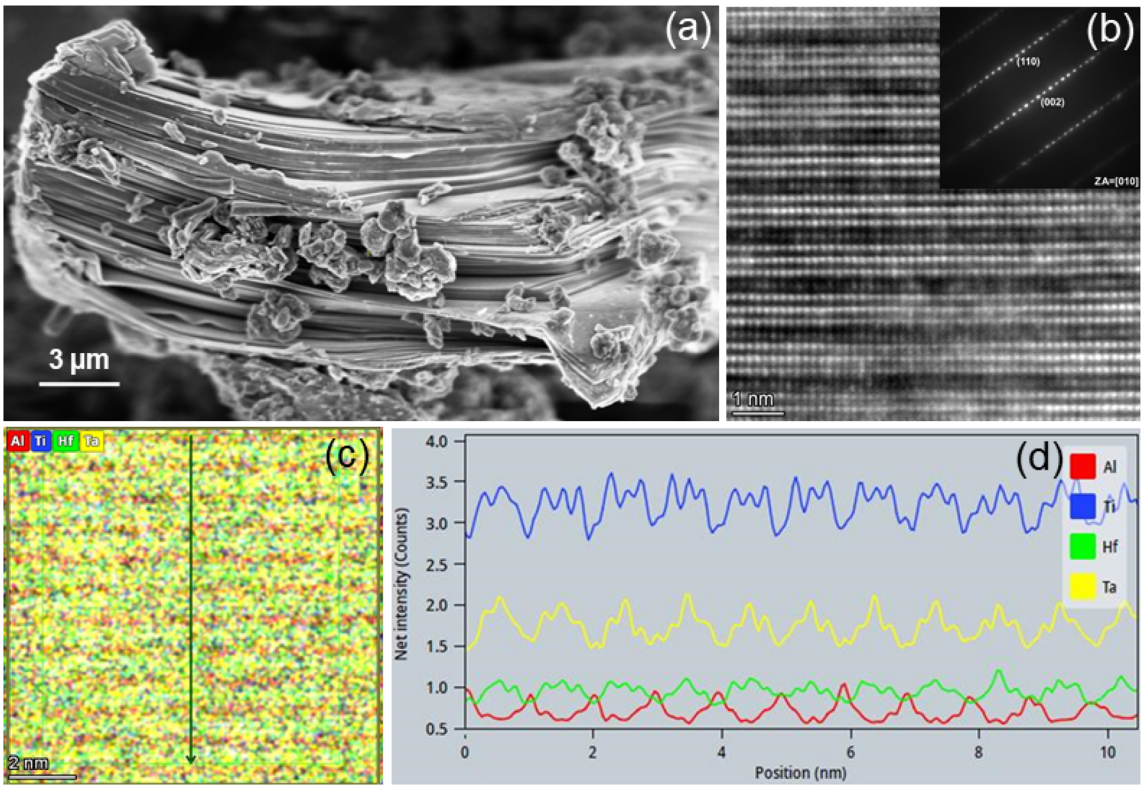

Fig. 2 Morphological and atomic scale characterization of $Ti_{2.7}Ta_{0.15}Hf_{0.15}AlC_2$ solid solution MAX phase. (a) The HR-SEM image of the $Ti_{2.7}Ta_{0.15}Hf_{0.15}AlC_2$ particle (b) atomic structure viewed along zone axis [010] of $Ti_{2.7}Ta_{0.15}Hf_{0.15}AlC_2$ using high resolution STEM, (c and d) EDS compositional line profiles obtained from elemental mapping.

substitutions, as these elements appear with brighter contrast compared to Ti in HAADF.

The chemical composition and surface elemental valence state of the Hf-substituted $Ti_{2.85}Hf_{0.15}C_2T_z$ and the Ta–Hf co-substituted $Ti_{2.7}Ta_{0.15}Hf_{0.15}C_2T_z$ MXenes were studied with XPS and shown in the Fig. 4. While XPS of Ta-substituted $Ti_3C_2T_z$ has previously been reported,[36] the addition of Hf and Ta–Hf (co-substitution) is expected to further alter the electronic structure of the metals within the flake.

Fig. 4(a) shows the Ti 2p core electron spectrum of in the Ta–Hf co-substituted $Ti_{2.7}Ta_{0.15}Hf_{0.15}C_2T_z$ with peaks characteristic for $Ti_3C_2T_z$-type MXenes. The peaks at binding energies (BEs) of 455.4 eV (Ti $2p_{3/2}$) and 461.2 eV (Ti $2p_{1/2}$) are attributed to Ti–C bonding. Moreover, the peaks at BE values of 456.7 eV and 462.5 eV, which correspond to the spin orbit coupling pair of Ti $2p_{3/2}$ and Ti $2p_{1/2}$, occurred due to the Ti–C_z bond (where z represents the –O, –F, and OH functional groups present at the surface of the MXene).[54,55] Further, the partially oxidized surface of the Ta–Hf co-substituted $Ti_{2.7}Ta_{0.15}Hf_{0.15}C_2T_z$ was observed at BE values of 459.1 eV and 464.8 eV, which correspond to the Ti–O bond, and is regularly observed in as-synthesized $Ti_3C_2T_z$.[56,57] Ta 4f and Hf 4f XPS spectra were deconvolved and shown in Fig. 4(b). Peaks at 14.3 eV (Hf $4f_{7/2}$) and 15.9 eV (Hf $4f_{5/2}$) are attributed to Hf–C bonding, whereas the peaks at 23.80 eV (Ta $4f_{7/2}$) and 25.74 eV (Ta $4f_{5/2}$) in the same spectrum are from Ta–C bonding.

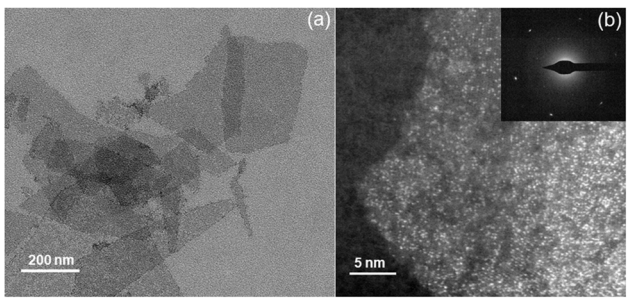

Fig. 3 Morphological and atomic scale characterization of the solid solution $Ti_{2.7}Ta_{0.15}Hf_{0.15}C_2T_z$ MXene. (a) TEM image the $Ti_{2.7}Ta_{0.15}Hf_{0.15}C_2T_z$ (b) The STEM image of single flake of MXene and corresponding SAED patterns in inset.

By comparison, XPS of Ti and Hf for the Hf-substituted (*i.e.*, no Ta) $Ti_{2.7}Hf_{0.3}C_2T_z$ are shown in Fig. 4(c) and (d), respectively. Importantly, the total Ti content remained the same in both samples. The metals in the as-synthesized Hf-substituted $Ti_{2.7}Hf_{0.3}C_2T_z$ MXene appear more oxidized compared to the co-substituted $Ti_{2.7}Ta_{0.15}Hf_{0.15}C_2T_z$ MXene, suggesting that the presence of Ta has a significant effect on the electronic structure. This effect was quantified by deconvoluting the XPS spectra and calculating how the relative fraction of M–C, M–O, and M–T_z bonding in as-synthesized MXenes varied between the unsubstituted ($Ti_3C_2T_z$), Ta-substituted ($Ti_{2.85}Ta_{0.3}C_2T_z$), Hf-substituted ($Ti_{2.7}Hf_{0.3}C_2T_z$), and Ta–Hf co-substituted ($Ti_{2.7}Ta_{0.15}Hf_{0.15}C_2T_z$) MXenes, as shown in Table 2.

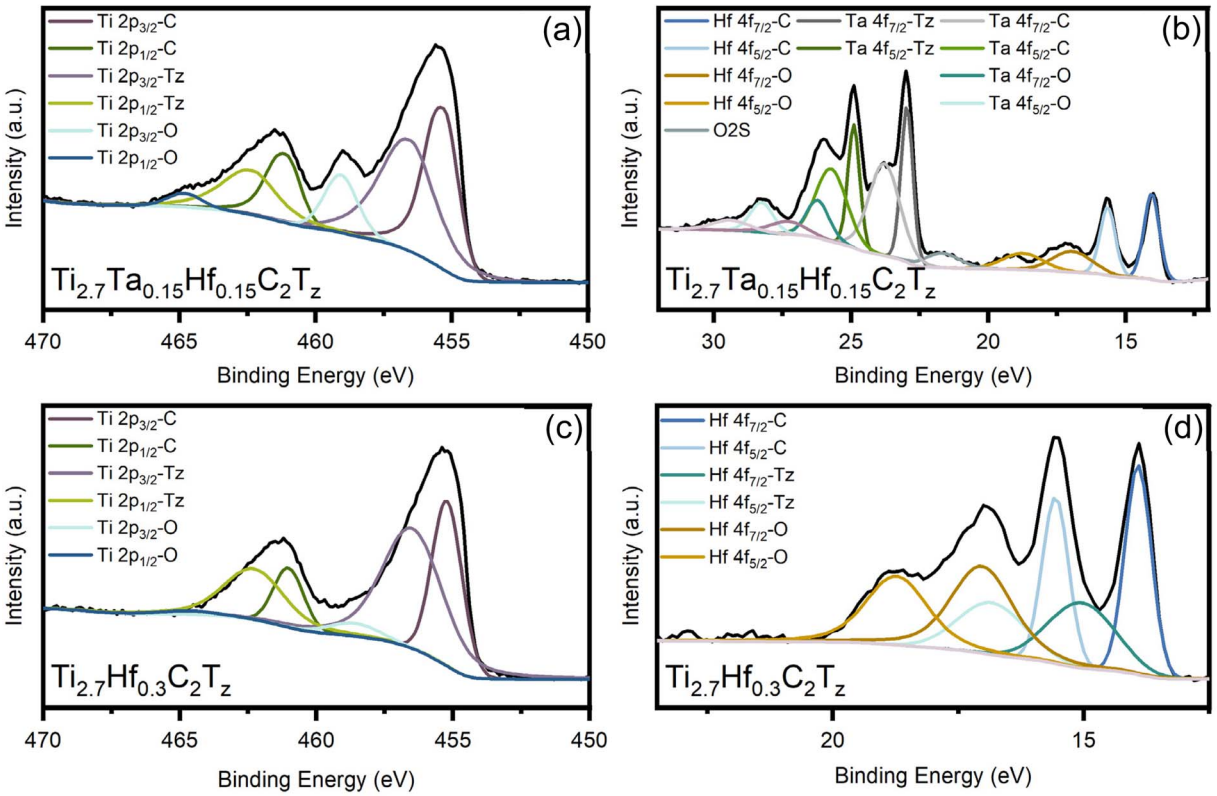

Fig. 4 XPS spectra for the $Ti_{2.7}Ta_{0.15}Hf_{0.15}C_2T_z$ and $Ti_{2.7}Hf_{0.3}C_2T_z$ core levels of (a) Ti 2p, (b) Ta 4f and Hf 4f, and the $Ti_{2.7}Hf_{0.3}C_2T_z$ core levels of (c) Ti 2p and (d) Hf 4f show different chemical environments.

XPS data revealed that in the Ti $2p_{3/2}$ spectrum, the Ti–C contribution decreased from 60.32% to 34.29% as a result of Hf substitution, while Ti–T_z increased from 35.17% to 60.70%, indicating enhanced termination coverage with Hf substitution. For the Ta-substituted $Ti_{2.7}Ta_{0.3}C_2T_z$, the Ti $2p_{3/2}$ comprised of 22.26% Ti–C, 59.8% Ti–T_z, and 17.94% Ti–O, reflecting increased termination coverage accompanied by a notable rise in oxide content relative to the unsubstituted sample. For the Ta–Hf co-substituted material, the Ti $2p_{3/2}$ components shifted to 41.08% Ti–C, 45.86% Ti–T_z, and 13.06% Ti–O, suggesting partial recovery of carbide bonding and reduced oxide content compared to the Ta-only case. In the Hf $4f_{7/2}$ region, $Ti_{2.7}Hf_{0.3}C_2T_z$ showed 37.85% Hf–O, 34.71% Hf–C, and 27.44% Hf–T_z, while in the case of the Ta–Hf co-substituted sample, Hf–C increased to 49.31% and Hf–O decreased to 24.99%, evidencing suppressed Hf oxidation when co-substituted with Ta. In the Ta $4f_{7/2}$ region, the Ta-only sample exhibited 78.98% Ta–T_z, 17.68% Ta–O, and 3.34% Ta–C, indicating that Ta strongly participated in termination bonding rather than forming carbides. The larger presence of termination bonds as measured by XPS can also be evidence of the inclusion of defects within the MXene upon doping.

In contrast, the Ta–Hf co-substituted material contained 47.47% Ta–C, 30.62% Ta–T_z, and 21.90% Ta–O, marking the emergence of carbide and termination-bound Ta alongside a modest decrease in Ta oxide compared to the Ta-only case. These changes support a cooperative effect in which oxyphilic Hf preferentially accommodates oxygen, while Ta stabilizes carbide and termination states, thereby suppressing bulk oxide growth and stabilizing the surface chemistry. This effect could be rationalized by the strong carbide stability of Ta and the high oxyphilicity of Hf, which drives Hf toward oxidation while Ta competes for oxygen and stabilized carbide/termination states,

Table 2 Fraction of the bonds of each metal in $Ti_3C_2T_z$, $Ti_{2.7}Ta_{0.3}C_2T_z$, $Ti_{2.7}Hf_{0.3}C_2T_z$ and $Ti_{2.7}Ta_{0.15}Hf_{0.15}C_2T_z$. M stands for metal, either Ti, Ta or Hf

Element	Ti $2p_{3/2}$				Ta $4f_{7/2}$		Hf $4f_{7/2}$	
Sample	Unsubstituted	Hf- substituted	Ta substituted	Ta–Hf	Ta-substituted	Ta–Hf	Hf-substituted	Ta–Hf
Bond	at%	at%	at%	co-substituted at%	at%	co-substituted at%	at%	co-substituted at%
M–C	60.32	34.29	22.26	41.08	3.34	47.47	34.71	49.31
M–O	4.50	5.00	17.94	13.06	17.68	21.90	37.85	24.99
M–T_z	35.17	60.70	59.80	45.86	78.98	30.62	27.44	25.69

altering oxide nucleation energetics, and promoting mixed terminations that suppress HfO_2 formation. This trend, therefore, suggests a synergistic effect between Ta and Hf, in which Ta stabilized Hf in its carbide form and suppressed its surface oxidation. Given the uncertainties associated with peak fitting and the surface sensitivity of XPS, the extracted bonding fractions should be treated as semi-quantitative. In addition, the electronic structure of the of the MXene mainly ruled by Ti 3d state near the fermi energy level, arising from strong hybridization between Ti 3d and C 2p orbitals.[58] This outcome high electrical conductivity but also localized electron density around Ti, which can act as a reactive center. Due to co-doping of Ta and Hf at the Ti site, substantial alteration of the electronic structure attributed to the introduction of more 5d orbitals. The hybridization between Ti 3d, Ta 5d, Hf 5d and C 2p states strengthen the M–C bond and widen the density of state near the Fermi level. This electronic modification reduces the density of high energy reactive centers and enhances the lattice stability. Moreover, co-substitution of Ta and Hf gives better electronic compensation to single metal doping. As a result, Ta and Hf co-substituted MXene phase shows improved structural robustness and better resistance to oxidation than that of pristine MXene.[59]

Accordingly, we focus on relative trends rather than absolute compositions. Based on these insights, the electrochemical corrosion behavior was subsequently investigated using potentiodynamic anodic polarization measurements.

Electrochemical oxidation and passivation behavior

Fig. 5 shows a comparison of potentiodynamic anodic corrosion curves of pristine $Ti_3C_2T_z$, Hf-substituted $Ti_{2.85}Hf_{0.15}C_2T_z$ $Ti_{2.7}Hf_{0.3}C_2T_z$, and Ta–Hf co-substituted $Ti_{2.85}Ta_{0.075}Hf_{0.075}C_2T_z$, and $Ti_{2.7}Ta_{0.15}Hf_{0.15}C_2T_z$, recorded at a potential scan rate of 0.167 mV s^{-1} in 0.5 M H_2SO_4 electrolyte solution. The calculated corrosion properties are summarized in Table 3.

The pristine $Ti_3C_2T_z$ exhibited the lowest corrosion potential (E_{corr}), indicating a thermodynamically higher susceptibility to anodic oxidation. Upon Ta–Hf co-substitution, E_{corr} shifted progressively toward more positive potentials, with increases of approximately 58 mV for $Ti_{2.85}Ta_{0.075}Hf_{0.075}C_2T_z$ and 94 mV for $Ti_{2.7}Ta_{0.15}Hf_{0.15}C_2T_z$ relative to pristine $Ti_3C_2T_z$. This positive shift reflects an enhanced resistance to the initiation of anodic corrosion and indicates improved electrochemical stability. In contrast, the Hf-only substituted MXenes showed E_{corr} values comparable to or lower than that of pristine $Ti_3C_2T_z$, suggesting that Hf substitution alone does not effectively delay the onset of oxidation and may even promote earlier anodic degradation under acidic conditions. Following the corrosion potential, pristine $Ti_3C_2T_z$ displayed a steep increase in anodic current density, characteristic of rapid oxidative degradation. This behavior is consistent with the known instability of $Ti_3C_2T_z$ at positive potentials, where oxidation of TiC bonds and surface terminations leads to the formation of electrochemically inactive TiO_2. By contrast, the Ta–Hf co-substituted MXenes exhibited significantly lower anodic current densities throughout the pre-passivation region. The reduced kinetic currents indicated suppressed oxidation rates, demonstrating that co-substitution effectively slowed the electrochemical degradation of the MXene lattice. The effect is more pronounced at higher substitution levels, highlighting a composition-dependent improvement in corrosion resistance. A distinct passivation plateau is observed for the Ta–Hf co-substituted MXenes, occurring at higher potentials compared to pristine and Hf-only substituted materials. The passivation potential (E_{pp}) increased by approximately 24 mV for $Ti_{2.85}Ta_{0.075}Hf_{0.075}C_2T_z$ and 31 mV for $Ti_{2.7}Ta_{0.15}Hf_{0.15}C_2T_z$ relative to pristine $Ti_3C_2T_z$. This shift indicates delayed formation of a stable passive layer and an expanded electrochemical stability window. The improved passivation behavior is attributed to the synergistic formation of stable Ta_2O_5 and HfO_2 surface oxides during anodic polarization. These oxides are known for their high thermodynamic stability and low solubility in acidic environments, enabling the formation of a protective barrier that limits further oxidation of the Ti-based MXene framework. In contrast, the Hf-only substituted MXenes showed earlier passivation but at higher passivation currents, suggesting the formation of less protective or partially soluble oxide layers that do not effectively inhibit continued anodic degradation. The superior performance of the Ta–Hf co-substituted MXenes

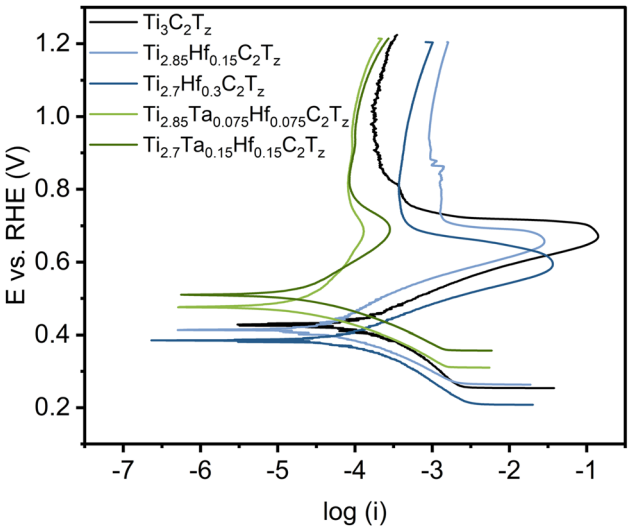

Fig. 5 Potentiodynamic anodic polarization curves for the native $Ti_3C_2T_z$, Hf-substituted $Ti_{2.85}Hf_{0.15}C_2T_z$, $Ti_{2.7}Hf_{0.3}C_2T_z$ and Ta–Hf co-substituted $Ti_{2.85}Ta_{0.075}Hf_{0.075}C_2T_z$, $Ti_{2.7}Ta_{0.15}Hf_{0.15}C_2T_z$ in N_2-saturated 0.5 M H_2SO_4 at a potential scan rate of 0.167 mV s^{-1}.

Table 3 Data derived from the potentiodyanamic anodic corrosion curves of as-synthesized materials

Sample name	E_{corr} [mV *vs.* RHE]	I_{corr} [μA]	E_{pp} [mV *vs.* RHE]	I_p[μA]
$Ti_3C_2T_z$	428	0.098	671.1	14.00
$Ti_{2.85}Ta_{0.075}Hf_{0.075}C_2T_z$	486	0.036	695.1	0.132
$Ti_{2.7}Ta_{0.15}Hf_{0.15}C_2T_z$	522	0.033	701.6	0.291
$Ti_{2.85}Hf_{0.15}C_2T_z$	423	0.025	656.8	28.44
$Ti_{2.7}Hf_{0.3}C_2T_z$	398	0.041	593.4	36.48

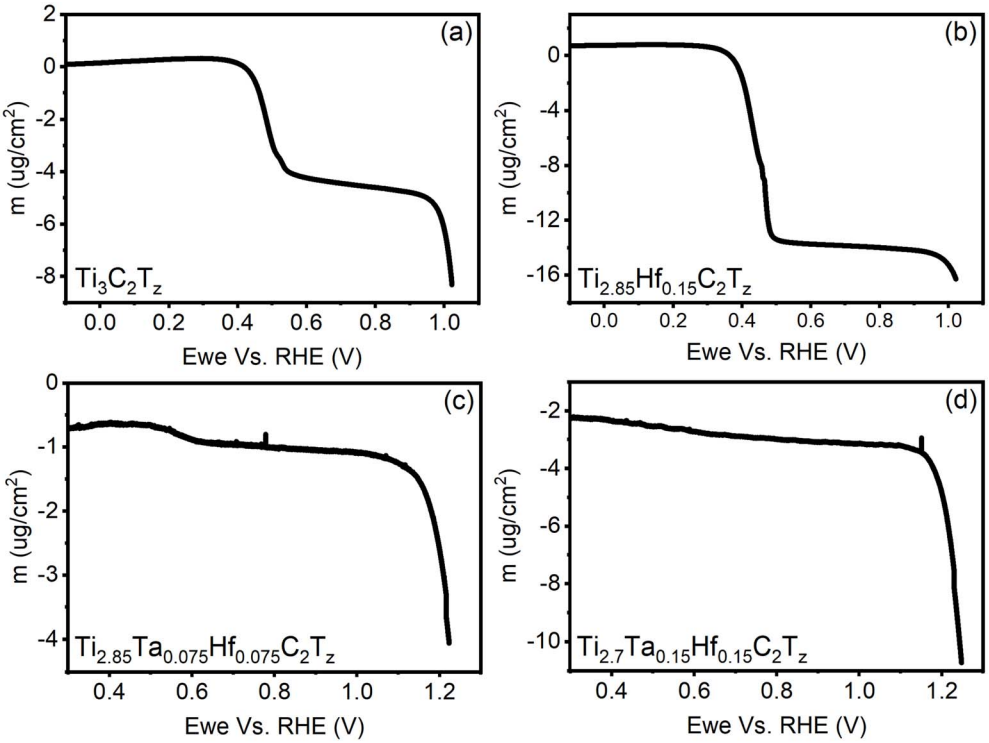

Fig. 6 (a) The comparative polarization curves of the $Ti_3C_2T_z$, $Ti_{2.85}Ta_{0.075}Hf_{0.075}C_2T_z$ and $Ti_{2.7}Ta_{0.15}Hf_{0.15}C_2T_z$ in N_2-saturated 0.5 M H_2SO_4 at a potential scan rate of 0.167 mV s^{-1} (b–d) change in mass *versus* potential for $Ti_3C_2T_z$, $Ti_{2.85}Ta_{0.075}Hf_{0.075}C_2T_z$ and $Ti_{2.7}Ta_{0.15}Hf_{0.15}C_2T_z$ single layer flakes drop casted on TiAu EQCM electrode.

arises from a cooperative effect between the two dopants. Hf, being highly oxyphilic, preferentially accommodates oxygen, while Ta stabilizes the carbide and termination environments and promotes the formation of a dense, adherent oxide layer. This synergy suppresses bulk Ti oxidation, reduces dissolution kinetics, and stabilizes the MXene surface under anodic polarization. The absence of similar improvements in Hf-only substituted MXenes highlights that enhanced corrosion resistance is not solely governed by oxyphilicity, but rather by the combined electronic and chemical stabilization afforded by co-substitution. Overall, the potentiodynamic anodic polarization curves demonstrate that Ta–Hf co-substitution substantially enhances the corrosion resistance, lowers anodic oxidation currents, and extends the passivation regime of $Ti_3C_2T_z$ MXenes in acidic media. These improvements directly translate into a wider electrochemical operating window, making TaHf co-substituted MXenes particularly attractive as durable electrocatalyst supports for applications such as PEM fuel cells, where exposure to high anodic potentials during start-up, shut-down, or fuel starvation is unavoidable.

An electrochemical quartz crystal microbalance (EQCM) was used to investigate change in mass of the electrode during the same potentiodynamic electrochemical oxidation of the $Ti_3C_2T_z$, $Ti_{2.85}Hf_{0.15}C_2T_z$, $Ti_{2.85}Ta_{0.075}Hf_{0.075}C_2T_z$, and $Ti_{2.7}Ta_{0.15}Hf_{0.15}C_2T_z$ as described above, the results of which are shown in Fig. 6.

EQCM measures apparent mass changes at the electrode surface during electrochemical cycling. Mass variations can be consistent with processes such as oxidation, dissolution, passivation, or ion adsorption. However, EQCM alone cannot distinguish between these mechanisms or identify the chemical nature of the surface species.[60] Therefore, the observed mass changes are interpreted cautiously and discussed in conjunction with the electrochemical data. The pristine $Ti_3C_2T_z$ and $Ti_{2.85}Hf_{0.15}C_2T_z$ revealed significant mass loss during the primary oxidation step due to the degradation of the surface functional groups (–O, –OH and –F), leading to the reduction in mass as shown in Fig. 6(a). In the case of the Hf-substituted MXene formation of amorphous HfO_2, which may have dissolved in the electrolyte with increase in potential as depicted in Fig. 6(b). Moreover, once reaching the primary passivation potential (E_{pp}), the mass stabilizes due to of the formation of a protective oxide layer.

Interestingly, there was no significant mass loss during the primary oxidation step in the case of the Ta–Hf co-substituted $Ti_{2.85}Ta_{0.075}Hf_{0.075}C_2T_z$ and $Ti_{2.7}Ta_{0.15}Hf_{0.015}C_2T_z$ as shown in Fig. 6(c and d). This is consistent with the potentiodynamic anodic polarization curves in Fig. 5, which showed significantly less oxidation current before reaching a passivation plateau. While the Hf-substituted MXene showed passivation behavior, the onset of oxidation was at significantly lower potentials, and the passivation currents were significantly higher compared to the Ta–Hf co-substituted MXene. This suggests that while Hf-substitution could slightly lower the passivation current compared to pristine MXene, only the co-substitution of Ta–Hf yielded improved performance with respect to arresting the

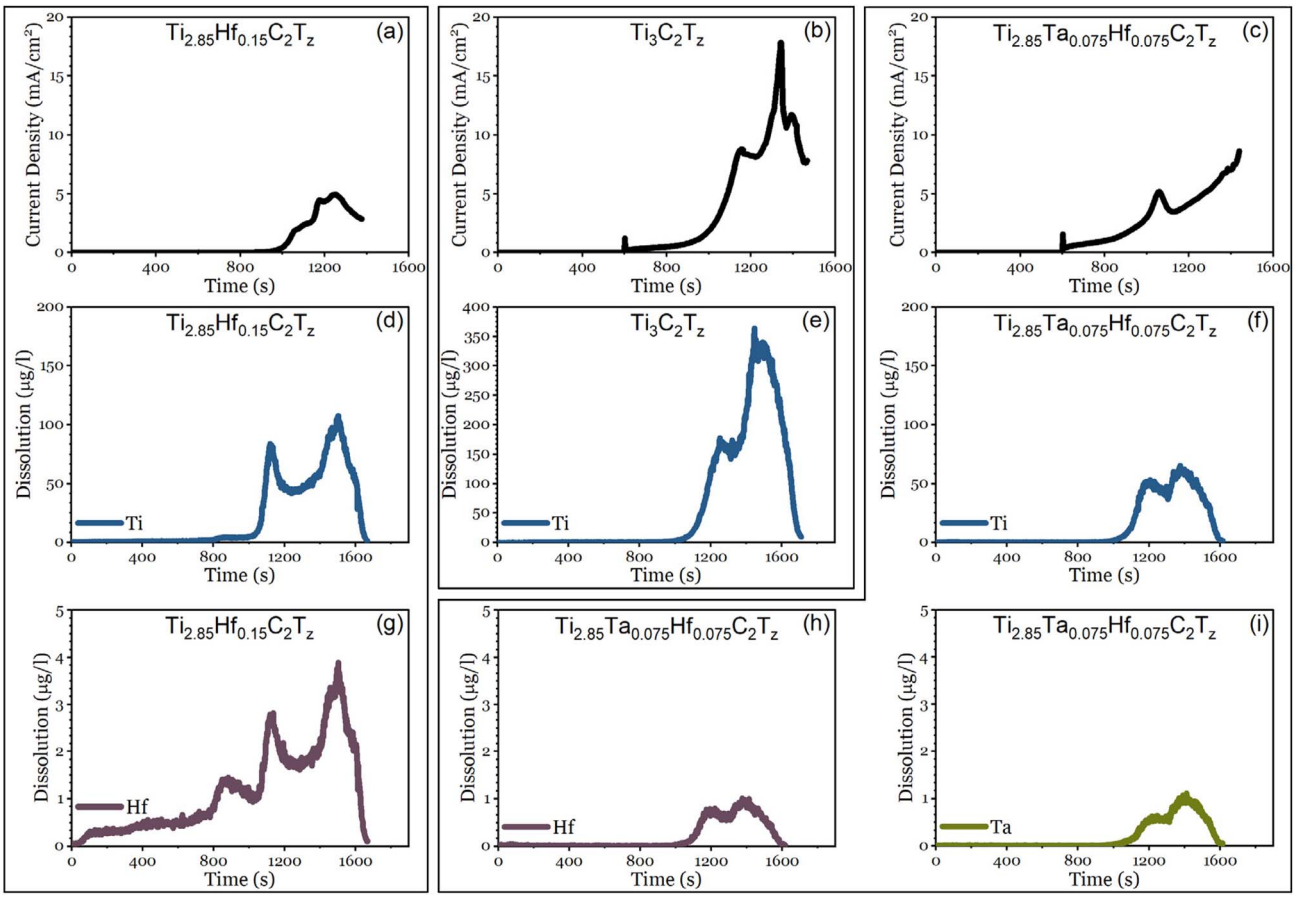

Fig. 7 *In situ* ICP-MS flow cell measurements of $Ti_3C_2T_z$ (a–d), $Ti_{2.85}$ $Hf_{0.15}C_2T_z$ (b, e and g), and $Ti_{2.85}$ $Hf_{0.075}Ta_{0.075}C_2T_z$ (c, f, h and i). (a–c) Current density, (d–f) Ti dissolution, (g,h) Hf dissolution, and (i) Ta dissolution. OCP (0.35 V *vs.* RHE) was held for 600 s and then ramped to 1.2 V *vs.* RHE at a rate of 1 mV s^{-1}.

oxidation process with increased electrochemical potential. DFT calculations have shown[55,61] that the dissociation enthalpy for Ta–O is slightly larger than that of Hf–O, and yet, the oxyphilicity of Ta was slightly lower than that of Hf, although quantitative comparison of oxyphilicity is limited by the lack of normalization data for Hf. Therefore, the stability resulting from the addition of Ta may be related to the stability of the formed oxides (*i.e.*, Ta_2O_5 and HfO_2), and less likely due to the inherent oxyphilicity of Ta by comparison to Hf.

Element-resolved corrosion and structural integrity

In-situ ICP-MS was used to track the water-soluble corrosion products of pristine, Hf-substituted and Ta–Hf co-substituted $Ti_3C_2T_z$ during potentiodynamic anodic polarization similar to the procedure used in Fig. 5. As seen from Fig. 7d ICP-MS of pristine $Ti_3C_2T_z$ showed significant Ti dissolution starting at 1025 s (0.7 V), in alignment with the increased current. The amount of Ti lost to anodic corrosion dropped significantly with Hf substitution (Fig. 7e), and even more significantly with Ta–Hf co-substitution (Fig. 7f) (at the same overall substitution level for Ti at the MXene with only Hf-substitution). Additionally, as seen in Fig. 7h, the amount of Hf measured by the ICP-MS noticeably dropped with the simultaneous addition of Ta. Importantly, the ICP-MS does not fully characterize the corrosion processes of the MXene flakes, but rather, only corrosion processes which lead to soluble corrosion products which are flushed away from the cell and fed into the ICP-MS. Metal leaching from electrodes during electrochemical operation is a significant barrier to electrode durability since its occurrence is typically irreversible. The ICP-MS result (as shown in Fig. 7f, h and i) of the Ta–Hf co-substituted MXene therefore suggests that the co-doping

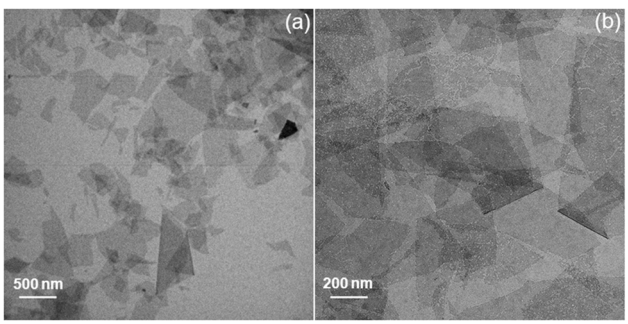

Fig. 8 (a) Bright-field TEM image of the pristine $Ti_{2.7}Ta_{0.15}Hf_{0.15}C_2T_z$. (b) Bright-field TEM images of the $Ti_{2.7}Ta_{0.15}Hf_{0.15}C_2T_z$ after scanning to the 0.9 V *vs.* RHE at 0.167 mV s^{-1} scan rate in the 0.5 M H_2SO_4.

strategy plays an important role in mitigating the overall corrosion (as described by the current density) and the formation of soluble corrosion products leading to irreversible damage, as shown by the metal content in the ICP-MS during anodic polarization. We believe that the mechanism by which the dissolution of Ti is reduced by the addition of Ta and Hf (and likewise the dissolution of Hf by the addition of Ta) has to do with favoring the forming non-soluble corrosion products based on Ta_2O_5 and HfO_2. This hypothesis comes from XPS, which indicates that the termination coverage and surface carbide composition (and hence corrosion product composition) varied dramatically upon Hf, Ta, and Hf-Ta co-substitution.

In order to corroborate chemical information, the structural effects of corrosion during potentiodyanamic anodic polarization was analyzed here using TEM and a technique reported by the authors previously.[36] Given the fact that the Ta–Hf co-substituted MXene showed the best performance in the potentiodynamic anodic polarization tests, $Ti_{2.7}Ta_{0.15}Hf_{0.15}C_2T_x$ was analyzed using TEM and shown in Fig. 8.

Fig. 8(a) shows the flakes of $Ti_{2.7}Ta_{0.15}Hf_{0.15}C_2T_z$ before electrochemical oxidation treatment whereas Fig. 8(b) and S6 shows the TEM and HR-TEM images of flakes after electrochemical corrosion testing conducted up to 0.9 V *vs.* RHE at a potential sweep rate of 0.167 mV s^{-1} in an acidic electrolyte (0.5 M H_2SO_4).

TEM shows that $Ti_{2.7}Ta_{0.15}Hf_{0.15}C_2T_z$ retained its original shape with edges remaining sharp and straight after electrochemical oxidation treatment. This contrasts with unsubstituted $Ti_3C_2T_z$ flakes reported by us[36] and others[34] whose edges and size undergo a dramatic change as a result of oxidation after the same (or similar) treatment. During oxidation of the Ta–Hf co-substituted MXene, 10–20 nm holes were observed on the basal plane of the flakes. The hole formation is likely associated with localized oxidation during anodic polarization, forming localized vacancies on its basal plane that served as initiation points for further oxidative attack rather than oxidation on its edges as seen in pristine MXene.[36] The occurrence of holes is due to the favored oxidation of Ta and Hf (compared to Ti), which altered how the flake oxidized and ultimately increased its durability under positive electrochemical potentials.

PEM fuel cell measurement

Finally, 40 wt% platinum was loaded on the as-synthesized MXenes, and designated here as Pt/$Ti_3C_2T_z$, Pt/

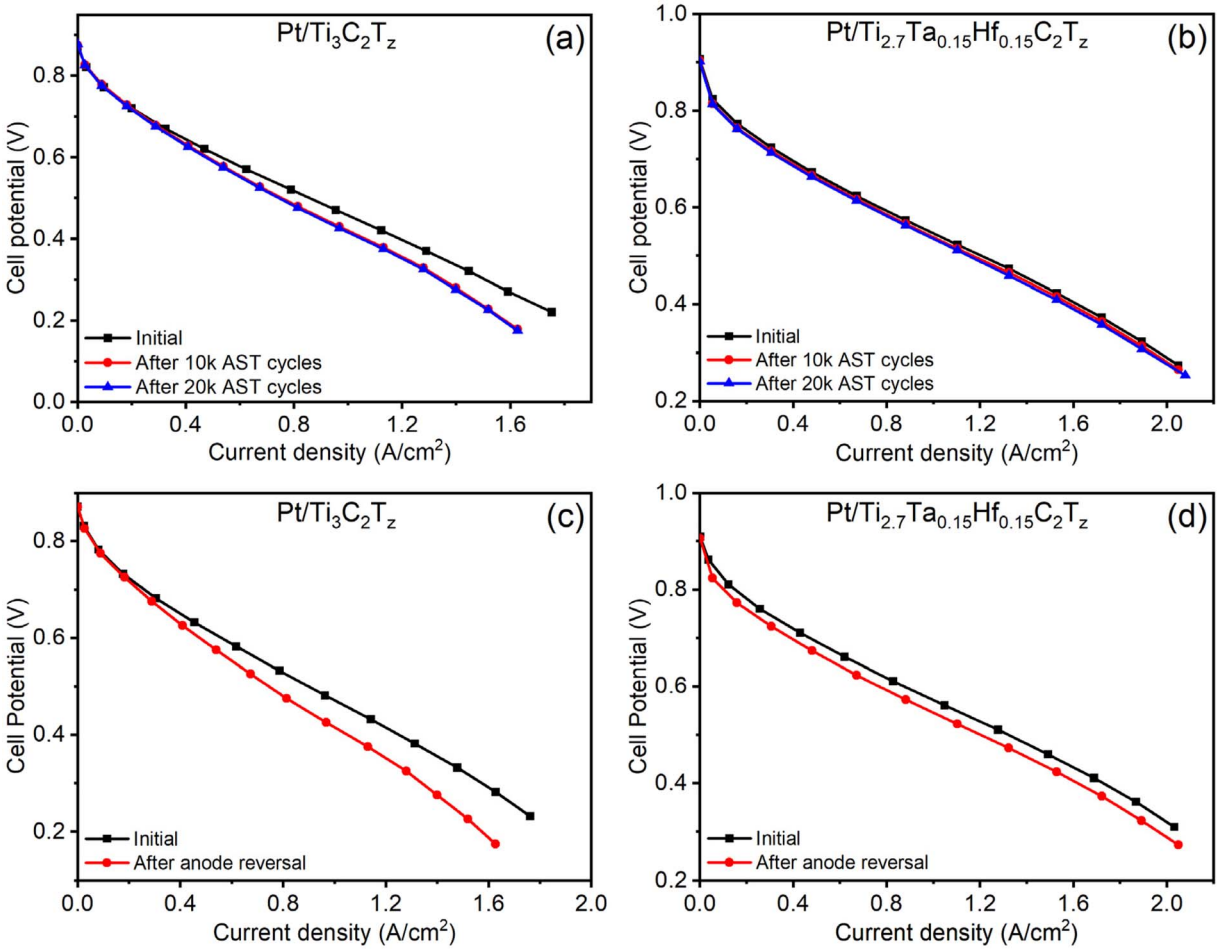

Fig. 9 Comparative AST polarization curves of fuel cell cycled between 0.6 to 0.9 V using state-of-the-art Pt/C cathode and Pt anode supported by (a) $Ti_3C_2T_z$ and (b) $Ti_{2.7}Ta_{0.15}Hf_{0.15}C_2T_z$. Polarization curves for 5 cm^2 fuel cell using Pt/C cathode and a Pt supported by (c) $Ti_3C_2T_z$ and (d) $Ti_{2.7}Ta_{0.15}Hf_{0.15}C_2T_z$ before and after anode reversal measurement.

$Ti_{2.85}Hf_{0.15}C_2T_z$, Pt/$Ti_{2.7}Hf_{0.3}C_2T_z$ Pt/$Ti_{2.85}Ta_{0.075}Hf_{0.075}C_2T_z$ and Pt/$Ti_{2.7}Ta_{0.15}Hf_{0.15}C_2T_z$. Pt loading on the MXene (Pt/$Ti_{2.7}Ta_{0.15}Hf_{0.15}C_2T_z$) flake was observed using TEM (Fig. S7). The TEM image shows the uniform distribution of Pt particles on the MXene flake, with an average particle size of 4.2 nm. A single-cell 5 cm^2 PEMFC was used to evaluate the performance of the variously substituted Pt-loaded MXene catalysts employed at the anode. While the use of the MXene at the anode does not completely parallel the corrosion tests reported above, owing to the flow of hydrogen, anode reversal tests simulating extreme fuel starvation were performed to reach the highly positive potentials known to cause degradation in PEMFCs during startup-up and shut-down operations.[62]

Fig. S8 shows the polarization curves of the Pt/$Ti_3C_2T_z$, Pt/$Ti_{2.85}Hf_{0.15}C_2T_z$, Pt/$Ti_{2.7}Hf_{0.3}C_2T_z$, Pt/$Ti_{2.85}Ta_{0.075}Hf_{0.075}C_2T_z$, and Pt/$Ti_{2.7}Ta_{0.15}Hf_{0.15}C_2T_z$. Among all the catalysts, Pt/$Ti_{2.7}Ta_{0.15}Hf_{0.15}C_2T_z$ showed substantially improved performance. This represents a significant accomplishment in catalyst support development, as the co-substituted MXene support shows both better performance and better durability, as shown in Fig. 5 and 6 and discussed further below. Typically, improvements in durability come at the expense of activity, and *vice versa*.[63,64]

The impact of Hf- and Ta-substitution on catalyst durability was tested using an accellerated stress test (AST), which included cycling the cell between 0.6 and 0.9 V for up to 20 k electrochemical cycles. The polarization curves before and after 20 k cycles of the Pt/$Ti_3C_2T_z$, Pt/$Ti_{2.7}Ta_{0.15}Hf_{0.15}C_2T_z$, Pt/$Ti_{2.85}Ta_{0.075}Hf_{0.075}C_2T_z$ and Pt/$Ti_{2.85}Ta_{0.15}C_2T_z$ when used as anode catalyst and commercially available Pt/C catalyst coated Nafion NR-212 membrane used as cathode in full cell are represented in Fig. 9, S9(a) and S10, respectively. As a result, after 20 k cycles, the Pt/$Ti_3C_2T_z$ supported anode was degraded by 39 mV, as shown in Fig. 9(a). Impressively, in the case of the Pt/$Ti_{2.7}Ta_{0.15}Hf_{0.15}C_2T_z$ (Fig. 9(b)) anode degradation was only 9 mV at 0.6 A cm^{-2} under the same electrochemical cycling test after 20 k cycles. In addition, Pt/$Ti_{2.7}Ta_{0.15}Hf_{0.15}C_2T_z$ exhibited a degradation trend comparable to that of Pt/$Ti_{2.85}Ta_{0.15}C_2T_z$ (Fig. S10), tested in our previous work.[36]

The anode reversal degradation test was performed to investigate the sustainability of the anode under severe fuel starvation. In this test, the anode side of the fuel cell was purged with humidified nitrogen (N_2) and a constant current density of 0.2 A cm^{-2} was applied, causing a sudden drop in cell voltage (*i.e.*, a dramatic increase in anode voltage). Furthermore, the system changes were monitored for 2 hours under the applied reversal condition. After the anode reversal test, the cell was conditioned, and the polarization curve was measured to evaluate the performance after the anode reversal test.

Fig. 9(c and d) and S9(b) show the polarization curves for Pt/$Ti_3C_2T_z$, $Ti_{2.7}Ta_{0.15}Hf_{0.15}C_2T_z$ and Pt/$Ti_{2.85}Ta_{0.075}Hf_{0.075}C_2T_z$ as the anode in the fuel cell before and after the anode reversal test, respectively. The results of the anode reversal sustainability study are consistent with those obtained from the AST test, indicating that Pt-loaded $Ti_{2.7}Ta_{0.15}Hf_{0.15}C_2T_z$ anode shows superior performance compared to $Ti_3C_2T_z$ supported Pt anode in a fuel cell. Moreover, TEM analysis was carried out to examine the surface changes of the electrocatalyst Pt/$Ti_{2.7}Ta_{0.15}Hf_{0.15}C_2T_z$ after 20 k AST. Fig. S11 reveals the TEM images of the Pt/$Ti_{2.7}Ta_{0.15}Hf_{0.15}C_2T_x$ after the AST test. Fig. S11 reveals no significant change in the morphology of the Pt/$Ti_{2.7}Ta_{0.15}Hf_{0.15}C_2T_z$, whereas Pt particles start to agglomerate, which confirms the stable nature of the catalyst.

Overall, all the results suggest that 10 at% co-substituted Ta and Hf MXene ($Ti_{2.7}Ta_{0.15}Hf_{0.15}C_2T_z$) shows significant enhancement in the electrochemical oxidation properties, which helps to improve the durability and sustainability of the support material in fuel cell technology.

Conclusions

$Ti_3C_2T_z$ MXenes were modified through hafnium substitution and tantalum–hafnium co-substitution to investigate how oxyphilic metal incorporation influences anodic electrochemical stability and durability. While single Hf substitution provided limited improvement, Ta–Hf co-substitution significantly suppressed anodic corrosion, reduced metal dissolution, and extended the electrochemical stability window to more positive potentials. *Operando* dissolution measurements and surface analysis reveal that co-substitution stabilizes the MXene surface chemistry by suppressing titanium oxide formation and promoting the formation of protective mixed oxides. When employed as catalyst supports in proton exchange membrane fuel cells, Pt-loaded Ta–Hf co-substituted MXenes exhibited markedly improved durability under accelerated stress testing and anode reversal conditions compared to pristine and singly substituted MXenes. These findings demonstrate that oxyphilic metal co-substitution is an effective and general materials design strategy to stabilize MXenes under anodic conditions, enabling their use as durable catalyst supports in fuel cell and other electrochemical energy conversion applications.

Author contributions

Haridas Parse and Danielle Sviri Belilty: conceptualization, experiments, data curation, validation, investigation, writing – original draft, review and editing. Bar Favelukis: investigation, review and editing. Mathias Krämer: ICP-MS experiment and analysis. Andrea M. Mingers: review and editing. Sukanta Chakrabartty: investigation. Noam Eliaz: review and editing. Baptiste Gault: review and editing. Dierk Raabe: review and editing. Maxim Sokol and Brian A. Rosen: funding, supervision, writing – review and editing.

Conflicts of interest

The authors declare no conflict of interest.

Data availability

The data supporting the findings of this study are available within the article and its supplementary information (SI). Additional data are available from the corresponding author upon reasonable request. Supplementary information:

additional XRD patterns, SEM-EDX images, TEM images, and accelerated stress tests. See DOI: https://doi.org/10.1039/d6ta00700g.

Acknowledgements

The authors wish to acknowledge funding by the Deutsche Forschungsgemeinschaft (DFG) grant (EL 869/1-1 RA 659/30-1) through the German Research Foundation (DFG). The authors acknowledge Dr George Levi, Dr Pini Shekhter, and Alexander Gordin from the Center for Nanoscience and Nanotechnology, Tel Aviv University, for TEM, STEM-EDS, ICP-MS, and XPS characterization. The authors also acknowledge Dr Nitzan Maman, Dr Alexander Upcher, and Dr Vladimir Ezersky from the Ilse Katz Institute for Nanoscale Science and Technology, Ben-Gurion University of the Negev, for FIB preparation and HR-TEM measurements.

References

1 E. R. Hamo and B. A. Rosen, Transition Metal Carbides as Cathode Supports for PEM Fuel Cells, *Nano Res.*, 2022, **1**, 10218–10233, DOI: 10.1007/s12274-022-4831-3.

2 M. Boni, C. S. Manikanta and V. Velisala, Experimental Evaluation of Proton Exchange Membrane Fuel Cell Performance with Sinusoidal Flow Channel Designs, *Int. J. Hydrogen Energy*, 2024, **53**, 1233–1241, DOI: 10.1016/j.ijhydene.2023.11.340.

3 J. C. Meier, C. Galeano, I. Katsounaros, J. Witte, H. J. Bongard, A. A. Topalov, C. Baldizzone, S. Mezzavilla, F. Schüth and K. J. J. Mayrhofer, Design Criteria for Stable Pt/C Fuel Cell Catalysts, *Beilstein J. Nanotechnol.*, 2014, 44–67, DOI: 10.3762/bjnano.5.5.

4 V. Celorrio, J. Flórez-Montaño, R. Moliner, E. Pastor and M. J. Lázaro, Fuel Cell Performance of Pt Electrocatalysts Supported on Carbon Nanocoils, *Int. J. Hydrogen Energy*, 2014, **39**, 5371–5377, DOI: 10.1016/j.ijhydene.2013.12.198.

5 B. M. Tackett, W. Sheng and J. G. Chen, Opportunities and Challenges in Utilizing Metal-Modified Transition Metal Carbides as Low-Cost Electrocatalysts, *Joule*, 2017, **11**, 253–263, DOI: 10.1016/j.joule.2017.07.002.

6 T. Binninger, E. Fabbri, R. Kötz and T. J. Schmidt, Determination of the Electrochemically Active Surface Area of Metal-Oxide Supported Platinum Catalyst, *J. Electrochem. Soc.*, 2014, **161**(3), H121–H128, DOI: 10.1149/2.055403jes.

7 J. C. Ortiz-Herrera, H. Cruz-Martínez, O. Solorza-Feria and D. I. Medina, Recent Progress in Carbon Nanotubes Support Materials for Pt-Based Cathode Catalysts in PEM Fuel Cells, *Int. J. Hydrogen Energy*, 2022, **47**(70), 30213–30224, DOI: 10.1016/j.ijhydene.2022.03.218.

8 H. Schulenburg, B. Schwanitz, N. Linse, G. G. Scherer, A. Wokaun, J. Krbanjevic, R. Grothausmann and I. Manke, 3D Imaging of Catalyst Support Corrosion in Polymer Electrolyte Fuel Cells, *J. Phys. Chem. C*, 2011, **115**(29), 14236–14243, DOI: 10.1021/jp203016u.

9 K. J. J. Mayrhofer, S. J. Ashton, J. C. Meier, G. K. H. Wiberg, M. Hanzlik and M. Arenz, Non-Destructive Transmission Electron Microscopy Study of Catalyst Degradation under Electrochemical Treatment, *J. Power Sources*, 2008, **185**(2), 734–739, DOI: 10.1016/j.jpowsour.2008.08.003.

10 N. Yoshimoto; Y. Niida; M. Egashira, et al; K.-S. Han; J.-W. Na - Instability of Pt/C Electrocatalysts in Proton Exchange Membrane Fuel Cells: A Mechanistic Investigation You May Also like Used Lithium Ion Rechargeable Battery Recycling Using Etoile-Rebatt Technology Kyoo-Seung Han and Dongil Na-Nonflammable Gel Electrolyte Containing Alkyl Phosphate for Rechargeable Lithium Batteries Preparation of LiMn2O4 at the Low Temperature of 250 Degrees Using a Novel Eutectic Self-Mixing Method This Content Was Downloaded from IP Address.

11 B. Randrianarizafy, P. Schott, M. Gerard and Y. Bultel, Modelling Carbon Corrosion during a PEMFC Startup: Simulation of Mitigation Strategies, *Energies*, 2020, **13**(9), 2338, DOI: 10.3390/en13092338.

12 Q. Shen, M. Hou, D. Liang, Z. Zhou, X. Li, Z. Shao and B. Yi, Study on the Processes of Start-up and Shutdown in Proton Exchange Membrane Fuel Cells, *J. Power Sources*, 2009, **189**(2), 1114–1119, DOI: 10.1016/j.jpowsour.2008.12.075.

13 L. Zhao, J. Zhu, Y. Zheng, M. Xiao, R. Gao, Z. Zhang, G. Wen, H. Dou, Y. P. Deng, A. Yu, Z. Wang and Z. Chen, Materials Engineering toward Durable Electrocatalysts for Proton Exchange Membrane Fuel Cells, *Adv. Energy Mater.*, 2022, **1**, 2102665, DOI: 10.1002/aenm.202102665.

14 Y. Liu, T. G. Kelly, J. G. Chen and W. E. Mustain, Metal Carbides as Alternative Electrocatalyst Supports, *ACS Catal.*, 2013, **7**, 1184–1194, DOI: 10.1021/cs4001249.

15 W. Kong, J. Deng and L. Li, Recent Advances in Noble Metal MXene-Based Catalysts for Electrocatalysis, *J. Mater. Chem. A*, 2022, **21**, 14674–14691, DOI: 10.1039/d2ta00613h.

16 A. Liu, X. Liang, X. Ren, W. Guan, M. Gao, Y. Yang, Q. Yang, L. Gao, Y. Li and T. Ma, Recent Progress in MXene-Based Materials: Potential High-Performance Electrocatalysts, *Adv. Funct. Mater.*, 2020, **1**, 2003437, DOI: 10.1002/adfm.202003437.

17 M. Naguib, M. Kurtoglu, V. Presser, J. Lu, J. Niu, M. Heon, L. Hultman, Y. Gogotsi and M. W. Barsoum, Two-Dimensional Nanocrystals Produced by Exfoliation of Ti 3AlC 2, *Adv. Mater.*, 2011, **23**(37), 4248–4253, DOI: 10.1002/adma.201102306.

18 C. Shi, M. Beidaghi, M. Naguib, O. Mashtalir, Y. Gogotsi and S. J. L. Billinge, Structure of Nanocrystalline Ti3 C2 MXene Using Atomic Pair Distribution Function, *Phys. Rev. Lett.*, 2013, **112**(12), 125501, DOI: 10.1103/PhysRevLett.112.125501.

19 A. V. Mohammadi, J. Rosen and Y. Gogotsi, The World of Two-Dimensional Carbides and Nitrides (MXenes), *Science*, 2021, **11**, eabf1581, DOI: 10.1126/science.abf1581.

20 S. Hong, J. K. El-Demellawi, Y. Lei, Z. Liu, F. Al Marzooqi, H. A. Arafat and H. N. Alshareef, Porous Ti3C2TxMXene Membranes for Highly Efficient Salinity Gradient Energy Harvesting, *ACS Nano*, 2022, **16**(1), 792–800, DOI: 10.1021/acsnano.1c08347.

21 J. Halim, S. Kota, M. R. Lukatskaya, M. Naguib, M. Q. Zhao, E. J. Moon, J. Pitock, J. Nanda, S. J. May, Y. Gogotsi and M. W. Barsoum, Synthesis and Characterization of 2D Molybdenum Carbide (MXene), *Adv. Funct. Mater.*, 2016, **26**(18), 3118–3127, DOI: 10.1002/adfm.201505328.

22 L. He, H. Zhuang, Q. Fan, P. Yu, S. Wang, Y. Pang, K. Chen and K. Liang, Advances and Challenges in MXene-Based Electrocatalysts: Unlocking the Potential for Sustainable Energy Conversion, *Mater. Horiz.*, 2024, **22**, 4239–4255, DOI: 10.1039/d4mh00845f.

23 M. Naguib, V. N. Mochalin, M. W. Barsoum and Y. Gogotsi, 25th Anniversary Article: MXenes: A New Family of Two-Dimensional Materials, *Adv. Mater.*, 2014, **26**(7), 992–1005, DOI: 10.1002/adma.201304138.

24 A. Iqbal, J. Hong, T. Y. Ko and C. M. Koo, Improving Oxidation Stability of 2D MXenes: Synthesis, Storage Media, and Conditions, *Nano Converg.*, 2021, **1**, 9, DOI: 10.1186/s40580-021-00259-6.

25 A. Lipatov, A. Goad, M. J. Loes, N. S. Vorobeva, J. Abourahma, Y. Gogotsi and A. Sinitskii, High Electrical Conductivity and Breakdown Current Density of Individual Monolayer Ti3C2Tx MXene Flakes, *Matter*, 2021, **4**(4), 1413–1427, DOI: 10.1016/j.matt.2021.01.021.

26 Y. Guan, M. Zhang, J. Qin, X. Ma, C. Li and J. Tang, Hydrophilicity-Dependent Distinct Frictional Behaviors of Different Modified MXene Nanosheets, *J. Phys. Chem. C*, 2020, **124**(25), 13664–13671, DOI: 10.1021/acs.jpcc.0c01551.

27 M. P. Bilibana, Electrochemical Properties of MXenes and Applications, *Adv. Sens. Energy Mater.*, 2023, **2**(4), 100080, DOI: 10.1016/j.asems.2023.100080.

28 Z. Zhang, C. Liu, Y. Dai, B. Liu, P. Guo, F. Tu, M. Ma, L. Shen, Z. Zhao, Y. Liu, Y. Zhang, L. Zhao and Z. Wang, Sandwich-Structured MXene/Carbon Hybrid Support Decorated with Pt Nanoparticles for Oxygen Reduction Reaction, *ACS Appl. Energy Mater.*, 2022, **5**(12), 14957–14965, DOI: 10.1021/acsaem.2c02479.

29 S. He, Q. Zhu, R. A. Soomro and B. Xu, MXene Derivatives for Energy Storage Applications, *Sustain. Energy Fuels*, 2020, **1**, 4988–5004, DOI: 10.1039/d0se00927j.

30 A. Lipatov, M. Alhabeb, M. R. Lukatskaya, A. Boson, Y. Gogotsi and A. Sinitskii, Effect of Synthesis on Quality, Electronic Properties and Environmental Stability of Individual Monolayer Ti3C2 MXene Flakes, *Adv. Electron. Mater.*, 2016, **2**(12), 1600255, DOI: 10.1002/aelm.201600255.

31 R. Thakur, A. Vahidmohammadi, J. Moncada, W. R. Adams, M. Chi, B. Tatarchuk, M. Beidaghi and C. A. Carrero, Insights into the Thermal and Chemical Stability of Multilayered V2CT: X MXene, *Nanoscale*, 2019, **11**(22), 10716–10726, DOI: 10.1039/c9nr03020d.

32 M. Krämer, B. Favelukis, A. A. El-Zoka, M. Sokol, B. A. Rosen, N. Eliaz, S. H. Kim and B. Gault, Near-Atomic-Scale Perspective on the Oxidation of Ti3C2Tx MXenes: Insights from Atom Probe Tomography, *Adv. Mater.*, 2024, **36**(3), 2305183, DOI: 10.1002/adma.202305183.

33 P. Nayak, M. Yang, Z. Wang, X. Li, R. Miao and R. G. Compton, Single-Entity Ti3C2Tx MXene Electro-Oxidation, *Appl. Mater. Today*, 2022, **26**, 101335, DOI: 10.1016/j.apmt.2021.101335.

34 J. Tang, T. S. Mathis, N. Kurra, A. Sarycheva, X. Xiao, M. N. Hedhili, Q. Jiang, H. N. Alshareef, B. Xu, F. Pan and Y. Gogotsi, Tuning the Electrochemical Performance of Titanium Carbide MXene by Controllable In Situ Anodic Oxidation, *Angew. Chem.*, 2019, **131**(49), 18013–18019, DOI: 10.1002/ange.201911604.

35 L. Lorencova, T. Bertok, E. Dosekova, A. Holazova, D. Paprckova, A. Vikartovska, V. Sasinkova, J. Filip, P. Kasak, M. Jerigova, D. Velic, K. A. Mahmoud and J. Tkac, Electrochemical Performance of Ti3C2Tx MXene in Aqueous Media: Towards Ultrasensitive H2O2 Sensing, *Electrochim. Acta*, 2017, **235**, 471–479, DOI: 10.1016/j.electacta.2017.03.073.

36 B. Favelukis, S. Chakrabartty, V. Kumar, S. H. Kim, A. El-Zoka, M. Krämer, D. Raabe, B. Gault, N. Eliaz, A. Natan, M. Sokol and B. A. Rosen, Improved Durability of Ti3C2Tz at Potentials above the Reversible Hydrogen Electrode by Tantalum Substitution, *Adv. Funct. Mater.*, 2024, **34**(10), 2309749, DOI: 10.1002/adfm.202309749.

37 W. Hong, B. C. Wyatt, S. K. Nemani and B. Anasori, Double Transition-Metal MXenes: Atomistic Design of Two-Dimensional Carbides and Nitrides, *MRS Bull.*, 2020, **1**, 850–861, DOI: 10.1557/mrs.2020.251.

38 B. Ratzker, B. Favelukis, M. Baranov, Y. Rathod, A. Greenberg, O. Messer, D. A. Goldstein, A. Upcher, V. Ezersky, N. Maman, I. Biran, V. Natu and M. Sokol, Synthesis of Ti1-XWx Solid Solution MAX Phases and Derived MXenes for Sodium-Ion Battery Anodes, *Adv. Funct. Mater.*, 2024, 2406499, DOI: 10.1002/adfm.202406499.

39 M. Han, K. Maleski, C. E. Shuck, Y. Yang, J. T. Glazar, A. C. Foucher, K. Hantanasirisakul, A. Sarycheva, N. C. Frey, S. J. May, V. B. Shenoy, E. A. Stach and Y. Gogotsi, Tailoring Electronic and Optical Properties of MXenes through Forming Solid Solutions, *J. Am. Chem. Soc.*, 2020, **142**(45), 19110–19118, DOI: 10.1021/jacs.0c07395.

40 F. L. Meng, Y. C. Zhou and J. Y. Wang, Strengthening of Ti2AlC by Substituting Ti with V, *Scr. Mater.*, 2005, **53**(12), 1369–1372, DOI: 10.1016/j.scriptamat.2005.08.030.

41 C. Zuo and C. Zhong, Screen the Elastic and Thermodynamic Properties of MAX Solid Solution Using DFT Procedue: Case Study on (Ti1-XVx)2AlC, *Mater. Chem. Phys.*, 2020, **250**, 123059, DOI: 10.1016/j.matchemphys.2020.123059.

42 L. Wang, M. Han, C. E. Shuck, X. Wang and Y. Gogotsi, Adjustable Electrochemical Properties of Solid-Solution MXenes, *Nano Energy*, 2021, **88**, 106308, DOI: 10.1016/j.nanoen.2021.106308.

43 M. Dahlqvist and J. Rosen, Predictive Theoretical Screening of Phase Stability for Chemical Order and Disorder in Quaternary 312 and 413 MAX Phases, *Nanoscale*, 2020, **12**(2), 785–794, DOI: 10.1039/c9nr08675g.

44 A. Rafieerad, W. Yan, K. N. Alagarsamy, A. Srivastava, N. Sareen, R. C. Arora and S. Dhingra, Fabrication of Smart Tantalum Carbide MXene Quantum Dots with Intrinsic Immunomodulatory Properties for Treatment of Allograft

Vasculopathy, *Adv. Funct. Mater.*, 2021, **31**(46), 2106786, DOI: 10.1002/adfm.202106786.

45 K. R. G. Lim, M. Shekhirev, B. C. Wyatt, B. Anasori, Y. Gogotsi and Z. W. Seh, Fundamentals of MXene Synthesis, *Nat. Synth.*, 2022, 601–614, DOI: 10.1038/s44160-022-00104-6.

46 H. B. Parse, I. Patil, A. Swami and B. Kakade, An Adept Approach to Convert Titanium Carbide to Titanium Nitride and It's Composite with N-Doped Carbon Nanotubes for Efficient Oxygen Electroreduction Kinetics, *Catal. Today*, 2021, **370**, 46–54, DOI: 10.1016/j.cattod.2020.11.019.

47 M. Alhabeb, K. Maleski, B. Anasori, P. Lelyukh, L. Clark, S. Sin and Y. Gogotsi, Guidelines for Synthesis and Processing of Two-Dimensional Titanium Carbide (Ti3C2Tx MXene), *Chem. Mater.*, 2017, **29**(18), 7633–7644, DOI: 10.1021/acs.chemmater.7b02847.

48 K. Shevchuk, A. Sarycheva, C. E. Shuck and Y. Gogotsi, Raman Spectroscopy Characterization of 2D Carbide and Carbonitride MXenes, *Chem. Mater.*, 2023, **35**(19), 8239–8247, DOI: 10.1021/acs.chemmater.3c01742.

49 A. D. Handoko, K. D. Fredrickson, B. Anasori, K. W. Convey, L. R. Johnson, Y. Gogotsi, A. Vojvodic and Z. W. Seh, Tuning the Basal Plane Functionalization of Two-Dimensional Metal Carbides (MXenes) to Control Hydrogen Evolution Activity, *ACS Appl. Energy Mater.*, 2018, **1**(1), 173–180, DOI: 10.1021/acsaem.7b00054.

50 V. Natu, R. Pai, O. Wilson, E. Gadasu, H. Badr, A. Karmakar, A. J. D. Magenau, V. Kalra and M. W. Barsoum, Effect of Base/Nucleophile Treatment on Interlayer Ion Intercalation, Surface Terminations, and Osmotic Swelling of Ti3C2TzMXene Multilayers, *Chem. Mater.*, 2022, **34**(2), 678–693, DOI: 10.1021/acs.chemmater.1c03390.

51 N. Goossens, B. Tunca, T. Lapauw, K. Lambrinou and J. Vleugels, MAX Phases, Structure, Processing, and Properties. In *Encyclopedia of Materials: Technical Ceramics and Glasses*, Elsevier, 2021, Vol. 1–3, pp 182–199. DOI: 10.1016/B978-0-12-818542-1.00015-1.

52 M. T. P. Rigby, V. Natu, M. Sokol, D. J. Kelly, D. G. Hopkinson, Y. Zou, J. R. T. Bird, L. J. Evitts, M. Smith, C. P. Race, P. Frankel, S. J. Haigh and M. W. Barsoum, Synthesis of New M-Layer Solid-Solution 312 MAX Phases (Ta1-: XTix)3AlC2(x = 0.4, 0.62, 0.75, 0.91 or 0.95), and Their Corresponding MXenes, *RSC Adv.*, 2021, **11**(5), 3110–3114, DOI: 10.1039/d0ra09761f.

53 M. Shekhirev, J. Busa, C. E. Shuck, A. Torres, S. Bagheri, A. Sinitskii and Y. Gogotsi, Ultralarge Flakes of Ti3C2TxMXene via Soft Delamination, *ACS Nano*, 2022, **16**(9), 13695–13703, DOI: 10.1021/acsnano.2c04506.

54 Y. Cao, Q. Deng, Z. Liu, D. Shen, T. Wang, Q. Huang, S. Du, N. Jiang, C. Te Lin and J. Yu, Enhanced Thermal Properties of Poly(Vinylidene Fluoride) Composites with Ultrathin Nanosheets of MXene, *RSC Adv.*, 2017, **7**(33), 20494–20501, DOI: 10.1039/C7RA00184C.

55 O. Mashtalir, M. Naguib, V. N. Mochalin, Y. Dall'Agnese, M. Heon, M. W. Barsoum and Y. Gogotsi, Intercalation and Delamination of Layered Carbides and Carbonitrides, *Nat. Commun.*, 2013, **4**, 1716, DOI: 10.1038/ncomms2664.

56 J. E. von Treifeldt, K. L. Firestein, J. F. S. Fernando, C. Zhang, D. P. Siriwardena, C. E. M. Lewis and D. V. Golberg, The Effect of Ti3AlC2 MAX Phase Synthetic History on the Structure and Electrochemical Properties of Resultant Ti3C2 MXenes, *Mater. Des.*, 2021, **199**, 109403, DOI: 10.1016/j.matdes.2020.109403.

57 Z. Tian, H. Tian, K. Cao, S. Bai, Q. Peng, Y. Wang and Q. Zhu, Facile Preparation of Ti3C2Tx Sheets by Selectively Etching in a H2SO4/H2O2 Mixture, *Front. Chem.*, 2022, **10**, DOI: 10.3389/fchem.2022.962528.

58 M. Khazaei, M. Arai, T. Sasaki, C. Y. Chung, N. S. Venkataramanan, M. Estili, Y. Sakka and Y. Kawazoe, Novel Electronic and Magnetic Properties of Two-Dimensional Transition Metal Carbides and Nitrides, *Adv. Funct. Mater.*, 2013, **23**(17), 2185–2192, DOI: 10.1002/adfm.201202502.

59 S. Kc, R. C. Longo, R. Addou, R. M. Wallace and K. Cho, Impact of Intrinsic Atomic Defects on the Electronic Structure of MoS 2 Monolayers, *Nanotechnology*, 2014, **25**(37), 375703, DOI: 10.1088/0957-4484/25/37/375703.

60 R. M. Wittman, R. L. Sacci and T. A. Zawodzinski, Elucidating Mechanisms of Oxide Growth and Surface Passivation on Zinc Thin Film Electrodes in Alkaline Solutions Using the Electrochemical Quartz Crystal Microbalance, *J. Power Sources*, 2019, **438**, 227034, DOI: 10.1016/j.jpowsour.2019.227034.

61 K. P. A. Kepp, Quantitative Scale of Oxophilicity and Thiophilicity, *Inorg. Chem.*, 2016, **55**(18), 9461–9470, DOI: 10.1021/acs.inorgchem.6b01702.

62 A. P. Soleymani, L. Bonville, C. Wang, S. Schaefer, J. Waldecker and J. Jankovic, Quantifying Key Parameters to Provide Better Understating of Microstructural Changes in Polymer Electrolyte Membrane Fuel Cells during Degradation: A Startup/Shutdown Case Study, *J. Power Sources*, 2023, **563**, 232807, DOI: 10.1016/j.jpowsour.2023.232807.

63 S. Saha, J. A. Cabrera Rodas, S. Tan and D. Li, Performance Evaluation of Platinum-Molybdenum Carbide Nanocatalysts with Ultralow Platinum Loading on Anode and Cathode Catalyst Layers of Proton Exchange Membrane Fuel Cells, *J. Power Sources*, 2018, **378**, 742–749, DOI: 10.1016/j.jpowsour.2017.12.062.

64 E. R. Hamo and B. A. Rosen, Improved Durability and Activity in Pt/Mo2C Fuel Cell Cathodes by Magnetron Sputtering of Tantalum, *Chemelectrochem*, 2021, **8**(16), 3123–3134, DOI: 10.1002/celc.202100591.